Geophys. J. Int. (2000) **141,** 43–56

Effects induced by an earthquake on its fault plane: a boundary element study

Maurizio Bonafede and Andrea Neri

Dipartimento di Fisica, viale Berti-Pichat 8, 40127, *Bologna, Italy. E-mail: bonafede@ibogfs.df.unibo.it*

Accepted 1999 October 7. Received 1999 July 15; in original form 1998 October 23

SUMMARY

Mechanical effects left by a model earthquake on its fault plane, in the post-seismic phase, are investigated employing the 'displacement discontinuity method'. Simple crack models, characterized by the release of a constant, unidirectional shear traction are investigated first. Both slip components—parallel and normal to the traction direction—are found to be non-vanishing and to depend on fault depth, dip, aspect ratio and fault plane geometry. The rake of the slip vector is similarly found to depend on depth and dip. The fault plane is found to suffer some small rotation and bending, which may be responsible for the indentation of a transform tectonic margin, particularly if cumulative effects are considered. Very significant normal stress components are left over the shallow portion of the fault surface after an earthquake: these are tensile for thrust faults, compressive for normal faults and are typically comparable in size to the stress drop. These normal stresses can easily be computed for more realistic seismic source models, in which a variable slip is assigned; normal stresses are induced in these cases too, and positive shear stresses may even be induced on the fault plane in regions of high slip gradient. Several observations can be explained from the present model: low-dip thrust faults and high-dip normal faults are found to be facilitated, according to the Coulomb failure criterion, in repetitive earthquake cycles; the shape of dip-slip faults near the surface is predicted to be upward-concave; and the shallower aftershock activity generally found in the hanging block of a thrust event can be explained by 'unclamping' mechanisms.

Key words: earthquakes, faults, models, stress.

INTRODUCTION

The importance of normal stress in determining the conditions for rock failure is well known from laboratory experiments and reasonably well described by the Coulomb failure criterion (e.g. Jaeger & Cook 1979; Fung 1965). Significant insight into the aftershock generation process has been achieved by applying the modified Coulomb criterion (e.g. Turcotte & Schubert 1982) to computed stress fields generated by dislocation events (e.g. Stein *et al.* 1992; King *et al.* 1994). Similar methods have also been employed to model complex faulting events in terms of quasi-static interactions amongst different fault segments (Nostro *et al.* 1997) and to evaluate changes in earthquake hazards due to failure of a nearby fault (Stein *et al.* 1997). Perfettini *et al.* (1999) found evidence that normal stress changes as a result of unclamping the fault may have even larger effects on fault instability than predicted by the Coulomb criterion, possibly due to fluid infusion over the fault, or the induction of creep phenomena.

Most of the research carried out until now has concentrated on the effects of dislocation events on nearby faults. The effect of a dislocation event on its own fault plane has received little attention. This may be partly due to mathematical problems related to the presence of non-integrable stress singularities inside fault edges when a constant slip is imposed, but it might also be ascribed to the erroneous belief that no normal stress should be generated by a shear fault on its own fault plane.

Modelling a fault as a shear dislocation crack (with assigned stress drop) avoids the former problem; however, analytical solutions obtained in a plane strain or anti-plane configuration (i.e. infinite in the strike direction), embedded in an unbounded homogeneous medium, provide no normal stress on the fault plane. The same holds for a vertical strike-slip dislocation in an anti-plane configuration, even when the presence of a free surface is accounted for. A more realistic model of a fault should take into account features such as the finite dimension of the fault plane, the presence of the free surface and a generic fault dip that may give rise to effects such as non-unidirectional slip in response to unidirectional traction release and may deform and stress the fault plane; it will be shown that these features can be responsible for small perturbations to fault geometry and for large normal stresses over the fault plane,

which have received little attention in previous papers. The present study aims to investigate how these features affect the fault behaviour in the post-seismic phase.

Okada (1992) gave the complete set of analytical solutions for rectangular, inclined, buried and non-buried dislocation surfaces with constant slip in the *strike, dip* and *normal* directions. Using these analytical solutions a numerical solution can be developed for the *crack* problem on a rectangular and plane fault surface of any type. The problem to be solved is that of computing the 2-D slip distribution over the fault plane caused by a given stress drop. Only shear dislocations will be considered in the following, in which slip is constrained to be parallel to the dislocation surface (that is, the normal component of slip is assumed to vanish). We use the Boundary Element Method, which is often applied in geophysics and mineral engineering (Crouch & Starfield 1983). Following this method, we divide the fault surface into many rectangular subsurfaces (termed 'elements'), each characterized by constant slip, described by Okada's solutions. Imposing a given stress drop at the mid-point of each subsurface we recover the slip of each fault element. The general distribution of slip over the entire fault plane is computed by interpolating these constant slip values of the elementary dislocations. The fault's behaviour is determined by the superposition of each element's behaviour. This model has been studied employing a FORTRAN 77 code. In particular, we analysed three problems for faults of various dips, depths and mechanisms:

(1) the slip distribution on the fault surface in response to a uniform and unidirectional traction release, taking into account faults with different geometries and different failure mechanisms;
(2) the deformation of the fault in the direction normal to the fault plane;
(3) the stress *normal* to the fault plane that rises after the earthquake.

The main results are as follows.

(1) When imposing a unidirectional traction release in the *strike* or *dip* direction, both components of slip are generally non-vanishing. Most of the slip is *parallel* to the direction of the released traction, but a minor component of slip is present, over the fault plane, even in the direction perpendicular to the released traction; this component is generally lower than 6 per cent of the maximum slip for a buried fault, but may be up to 20 per cent for a fault reaching the free surface.
(2) A deformation of the fault surface is found that is caused by the displacement component normal to the fault plane. This displacement can be 15–25 per cent of the maximum slip.
(3) The deformation of the fault plane is accompanied by a stress component normal to the fault plane that can be compressive or extensional, depending on the fault mechanism, angle of dip and depth below the free surface. This normal stress is absent on vertical faults (due to the symmetry of the problem) and on very deep faults. The intensity of the normal stress is non-negligible, particularly for dip-slip faults, where it may reach 50 per cent of the stress drop for buried faults and up to 120 per cent for faults reaching the free surface.

The importance of this self-induced normal stress has been recently considered in dynamic simulations (numeric and analogue models) of near-source ground motion; these show significantly different modes of behaviour between thrust faults and normal faults, which are ascribed to time-dependent normal stresses, generated from the interaction of the fault with the free surface, which are asymmetric for normal and thrust faults (Oglesby *et al.* 1998; Shi *et al.* 1998). In the present paper we demonstrate that these effects are present even in static models, and large normal stresses are permanently left on the shallow section of a fault plane after an earthquake.

The role of a slowly increasing normal stress, related to the slow build-up of tectonic stress, is similarly found to be important in modelling the earthquake cycles on non-optimally oriented, vertical strike-slip faults (Becker & Schmeling 1998). The present paper provides a general overview of these effects depending on the fault depth, dip angle, aspect ratio and slip mechanism.

REFERENCE SYSTEMS AND CONVENTIONS

The results will be referred to the *general* system of coordinates (x, y, z) and to the *local* system (s, d, t), consistent with Okada's (1992) formalism (Fig. 1). Axes s, d, t are defined as the *strike, dip* and *normal* (pointing towards the free surface) directions, respectively.

The origin and x, y axes of the system (x, y, z) are on the free surface of the half-space and the z axis is upwards. The fault plane has a dip angle δ, positive in a counterclockwise direction, as shown in Fig. 1. The fault plane dimensions are L in the s direction and W in the d direction. In plots showing the dependence of quantities on the angle of dip we shall keep fixed the depth of the upper edge of the fault plane while varying the dip.

We define n^+ as the normal to the upper fault face, Σ^+, and n^- as the normal to the lower fault face, Σ^-. The n^+ vector also defines the direction of the t axis of the local system (s, d, t) (Fig. 1). Traction values given in the following paragraphs refer to the upper fault face Σ^+.

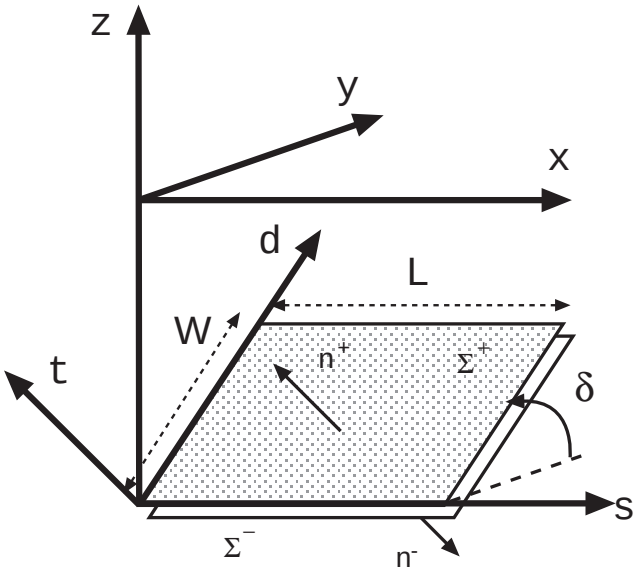

Figure 1. Sketch of the geometry of the problem and reference systems. The positive orientation n^+ of the fault plane Σ^+ is defined as that pointing into the hangingwall.

For the slip vector, D_i, we use the convention

$$D_i = \lim_{t\to 0^+} u_i - \lim_{t\to 0^-} u_i\,, \quad i = s, d, t\,,$$

where u_i is the displacement in the local system s, d, t. According to this convention, used by Okada (1992), if $D_s > 0$ ($D_d > 0$), the upper fault face Σ^+ moves towards the positive direction of the s (d) axis with respect to the lower face Σ^-. Thus, for $0^\circ < \delta < 90^\circ$, $D_s > 0$ means a left-lateral strike-slip fault, $D_s < 0$ a right-lateral strike-slip fault, $D_d > 0$ a thrust fault and $D_d < 0$ a normal fault. In the following, only shear faults will be considered, in which the normal opening is constrained to vanish, i.e. $D_t = 0$.

The following elastic constants are employed for the elastic half-space:

$$\lambda = \mu = 5 \times 10^{10}\ \text{Pa}\,,$$

as assumed by Press (1965) and Kasahara (1981), whose results were employed as control tests. The following fault dimensions will generally be employed, unless stated otherwise:

$$L = 12\ \text{km}\,, \qquad W = 8\ \text{km}\,,$$

as assumed in an example given by Okada (1992).

METHOD OF SOLUTION

The *displacement discontinuity* method, one of the boundary element techniques, is used to solve the crack problem. We consider a rectangular *shear*-fault with a dip angle δ and divide it into $M \times N$ rectangular dislocations, which we shall term *elements* in the following; an ordinal number $k = 1, \ldots, M \times N$ is assigned to each element; the kth element is characterized by *unknown* constant slip in the *strike* and *dip* directions:

$$\mathbf{D}^k = (D_s^k, D_d^k)\,, \qquad k = 1, \ldots, M \times N\,.$$

We impose the condition that the slip in the *normal* direction is zero:

$$D_t^k = 0\,, \qquad k = 1, \ldots, M \times N\,. \tag{1}$$

Looking at the fault surface from the $t > 0$ direction, k grows from the left to the right in the *strike* direction and from the bottom to the top in the *dip* direction. In this way the element in the lower left fault corner is assigned an ordinal number $k = 1$ and that in the upper right corner is assigned $k = M \times N$ (Fig. 2). Two fault mechanisms will be considered in the following, in which a unidirectional traction release, constant all over the fault surface, will be imposed:

$$\text{strike model}: \begin{cases} \Delta\sigma_s = 25\ \text{bar} \\ \Delta\sigma_d = 0\ \text{bar} \end{cases}, \quad \text{dip model}: \begin{cases} \Delta\sigma_s = 0\ \text{bar} \\ \Delta\sigma_d = 25\ \text{bar} \end{cases}, \tag{2}$$

where the subscripts s and d indicate the *strike* and *dip* directions. The free-surface condition in $z = 0$ and the conditions (1) and (2) over the fault surface are the boundary conditions for the problem to be solved.

Consider the generic kth element. Employing Okada's solutions, it is possible to compute the total traction, say $\mathbf{t}'^{(k)}$, induced on the kth element from the slip of all elements. The traction release can be written as a function of the *initial* traction, $\mathbf{t}^{0(k)}$, and the *final* traction, $\mathbf{t}^{\text{fin}(k)}$, in the following way:

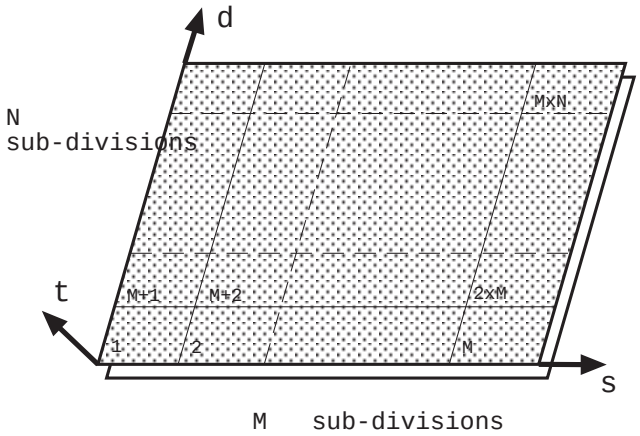

Figure 2. Fault plane subdivision into $M \times N$ rectangular elements, each characterized by a constant slip ($D_s^{(k)}$, $D_d^{(k)}$). Each element is identified through its ordinal number k.

$$\begin{cases} \Delta t_s^{(k)} = t_s^{0(k)} - t_s^{\text{fin}(k)} \\ \Delta t_d^{(k)} = t_d^{0(k)} - t_d^{\text{fin}(k)} \end{cases}, \tag{3}$$

where

$$\mathbf{t}^{\text{fin}(k)} = \mathbf{t}^{0(k)} + \mathbf{t}'^{(k)}\,. \tag{4}$$

Substituting (4) into (3) we obtain

$$\begin{cases} \Delta t_s^{(k)} = -\,t_s'^{(k)} \\ \Delta t_d^{(k)} = -\,t_d'^{(k)} \end{cases}. \tag{5}$$

More specifically, the total traction $\mathbf{t}'^{(k)}$ induced on the kth element is obtained by summing the tractions $\mathbf{t}^{(i)}$ produced by each ith element computed on the central point $CP(k)$ of the kth element. Therefore,

$$\mathbf{t}'^{(k)} = \sum_{i=1}^{M\times N} \mathbf{t}^{(i)}|_{CP(k)}\,.$$

The expression of $\mathbf{t}^{(i)}$ is *linear* in the slip components (D_s^k, D_d^k), $k = 1, \ldots, M \times N$, since Okada's solutions are linear in the slip components. Writing (4) for each element we obtain a linear system containing $2 \times M \times N$ equations in the $2 \times M \times N$ unknowns (D_s^k, D_d^k):

$$\begin{cases} t_s'^{(k)} = -\Delta t_s^{(k)} = \displaystyle\sum_{i=1}^{M\times N} A_{ss}^{ik} D_s^i + \sum_{i=1}^{M\times N} A_{sd}^{ik} D_d^i \\ t_d'^{(k)} = -\Delta t_d^{(k)} = \displaystyle\sum_{i=1}^{M\times N} A_{ds}^{ik} D_s^i + \sum_{i=1}^{M\times N} A_{dd}^{ik} D_d^i \end{cases}, \tag{6}$$

$k = 1, \ldots, M \times N$,

where A_{ss}, A_{sd}, A_{ds}, A_{dd} are matrices with $(M \times N)$ rows and $(M \times N)$ columns containing the *influence coefficients* of the traction that are computed using Okada's solutions. For example, A_{sd}^{ik} means the influence coefficient of the t_s' traction component on $CP(k)$ due to unit slip in the d direction at the ith element. Tractions $t_s'^{(k)} \ldots t_d'^{(k)} \ldots$ have been computed on the central point of each element in order to keep as far away as possible from the singularities present on element edges (Okada 1992).

Also, the third traction component, t'_t, normal to the fault plane, can be written as a function of the normal traction generated by each element:

$$t'^{(k)}_t = \sum_{i=1}^{M\times N} t^{(i)}_t|_{CP(k)} .$$

Thus, the total normal traction as a function of the slip $\mathbf{D}^i$, $i=1, \ldots, M\times N$, is

$$t'^{(k)}_t = \sum_{i=1}^{M\times N} A^{ik}_{ts} D^i_s + \sum_{i=1}^{M\times N} A^{ik}_{td} D^i_d , \qquad k=1, \ldots, M\times N . \qquad (7)$$

It is not possible to impose any condition on this normal component of traction because the system (6) is already completely determined, having imposed the condition $D^{(k)}_t = 0$, $k=1, \ldots, M\times N$. Therefore, in general, a field of normal stress is induced by a shear slip alone.

Solving the system (6) allows us to compute the distribution of slip $\mathbf{D}^{(k)}$, $k=1, \ldots, M\times N$, on the fault plane, for a given distribution $\Delta t^{(k)}_s$ and $\Delta t^{(k)}_d$, defined on fault elements. Then, using (7), we can compute the normal traction t'_t. From the slip distribution it is also possible to evaluate the displacement field, u_t normal to the fault plane, employing the following relation:

$$u^{(k)}_t = \sum_{i=1}^{M\times N} U^{ik}_{ts} D^i_s + \sum_{i=1}^{M\times N} U^{ik}_{td} D^i_d , \quad k=1, \ldots, M\times N , \qquad (8)$$

where U^{ik}_{ts}, U^{ik}_{td} are matrices containing the normal displacement influence coefficients, computed from Okada's (1992) solutions. For these matrices the notation is the same as for matrices of traction influence coefficients.

Continuous displacement components u_s, u_d have been computed on the fault plane following Okada (1992) as the average value of each fault face displacement:

$$u_i|_\Sigma = (u_i|_{\Sigma^+} + u_i|_{\Sigma^-})/2 .$$

They are found to be generally smaller than u_t. Their pattern is very similar to that of the slip component they are parallel to which is always greater by about one order of magnitude. Thus, the slip components are mostly responsible for the displacement field parallel to the fault plane. However, the derivatives $\partial u_s/\partial s$ and $\partial u_d/\partial d$ are involved in the computation of t'_t.

Because of the linearity in the slip components of the system (6) and eqs (7) and (8), faults having the same slip components in absolute value but of opposite sign develop tractions and displacements that differ only in sign. This happens, for example, for a normal and a thrust fault with the same dip and stress drop.

The numerical procedure described above has been tested comparing the analytical solution for a vertical crack in an elastic half-space extending indefinitely in the strike direction (Knopoff 1958) with the numerical solution for the same problem. The analytical solution gives the strike-slip component D_s as a function of the depth z for a given stress drop. To find the numerical solution for this problem we use a fault with $L/W \gg 1$ to simulate a fault of infinite extent in the strike direction, and divide it into N strips with dimensions $(L, W/N)$ and unknown slip $\mathbf{D}^k$, $k=1, N$, to reproduce the slip dependence on z. We obtained very good agreement, and, as expected, the numerical solution improves as the fault plane subdivision is refined more and more (Fig. 3). In the calculations we use a model with $M\times N = 10\times 10$ elements as a reasonable compromise between the requirement of accuracy and computational efficiency.

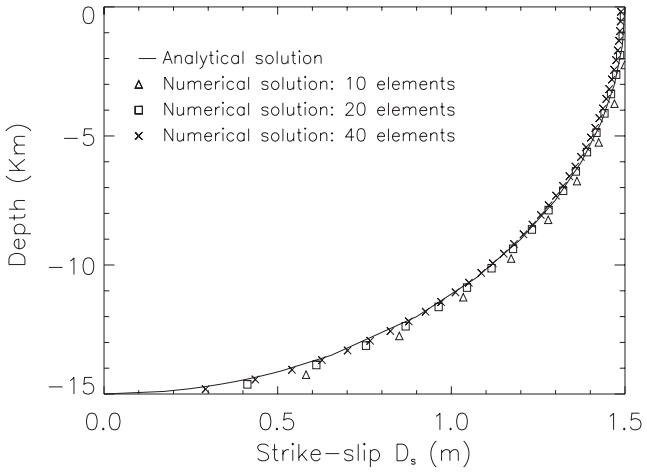

Figure 3. Comparison of the analytical solution (solid line) for a strike-slip crack in anti-plane configuration (Knopoff 1958) and numerical solutions for a 'very long' crack (symbols) obtained with an increasing number of elements.

SLIP DISTRIBUTION

In the following, by *strike-slip* fault we mean a fault releasing traction in the *strike* direction and by *dip-slip*, a fault releasing traction in the *dip* direction. In order to present the results we define the following:

(1) $D_\parallel$: slip component *parallel* to the released traction ($D_\parallel = D_s$ for strike-slip faults; $D_\parallel = D_d$ for dip-slip faults);
(2) $D_\perp$: slip component *normal* to the released traction ($D_\perp = D_d$ for strike-slip faults; $D_\perp = D_s$ for dip-slip faults).

Figs 4 and 5 show the two components of slip on faults with traction release in the *strike* and *dip* directions, respectively. The maximum slip is obtained for the $D_\parallel$ component. This has its maximum in the central part of the fault surface and goes to zero towards the edges, where the fracture closes. However, a slip component normal to the released traction is present in general, with relative maxima near the upper fault corners. The location of $D_\perp$ near these corners is clearly due to the fact that the slip vector there has high gradients, being constrained to vanish at and above the upper fault rim while the bottom rim is far away. To show this more clearly, in Fig. 6 a strike-slip rectangular fault is considered, with a 3 MPa stress drop over a central asperity, while the rest of the fault is left free to slip with vanishing stress drop. Fig. 6(b) shows that the $D_\perp$ maxima are located in regions where the slip gradient is high, rather than at fault rims.

A trapezoidal strike-slip fault model was also considered, by imposing the condition that the slip vanishes on a triangle next to the top right corner (Fig. 7). A comparison with the rectangular fault of Fig. 4 shows that the oblique angle under which the released traction sees the fault border deflects $D_\perp$ diagonally downwards. $D_\perp$ maxima, however, are similar (in absolute value) to those in Fig. 4.

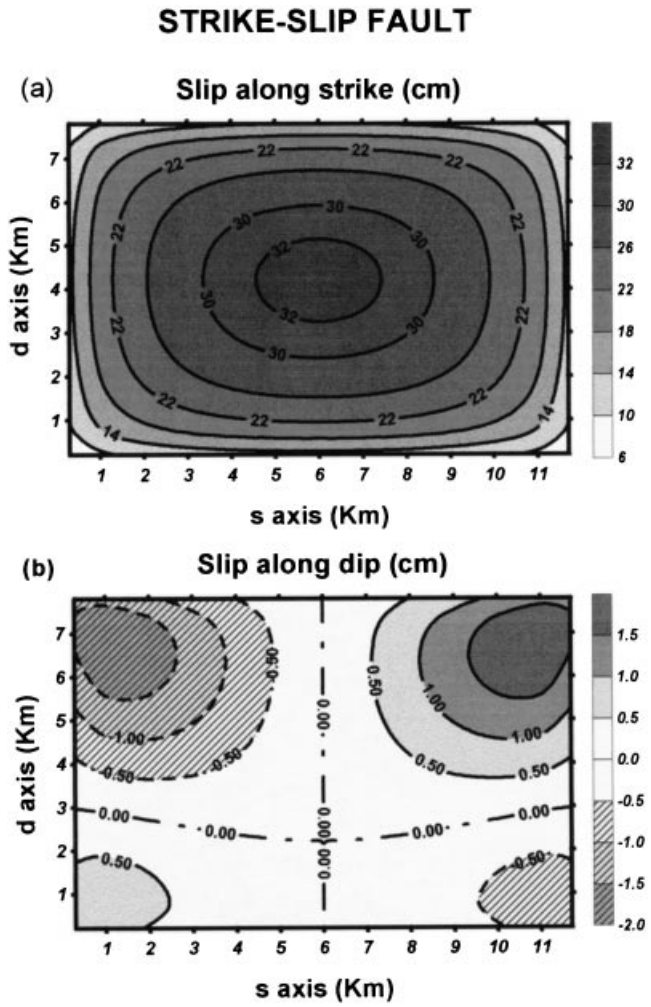

Figure 4. Slip along strike (a) and dip (b) for a rectangular fault with upper edge at a depth of 1 km and releasing 2.5 MPa in the strike direction with dip angle 60°. The fault dimensions are $L=12$ km, $W=8$ km.

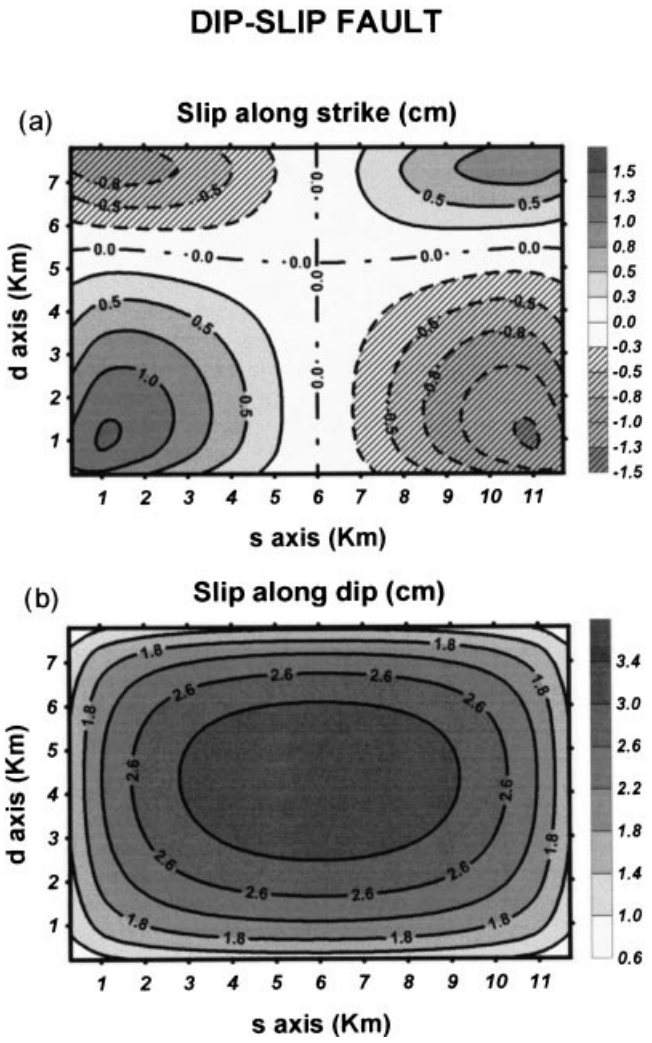

Figure 5. Slip along strike (a) and dip (b) for a rectangular fault with upper edge at a depth of 1 km and releasing 2.5 MPa in the dip direction with dip 30°. The fault dimensions are $L=12$ km, $W=8$ km.

Thus, even if a unidirectional traction is released, both components of fault slip are non-vanishing, instead of only one component in the *strike* or *dip* direction (as provided by plane strain or anti-plane fault models).

The component $D_\perp$ is found to be typically small but it increases as the fault depth decreases. For a buried fault, we find

$$R_1 = \frac{\max|D_\perp|}{\max|D_\parallel|} \approx 3-5 \text{ per cent},$$

while, if the fault reaches the free surface,

$$R_1 = \frac{\max|D_\perp|}{\max|D_\parallel|} \approx 8-20 \text{ per cent}.$$

In Figs 8(a) and (b), the ratio R_1 is plotted against the dip angle for different fault depths for strike-slip and dip-slip models respectively. Curves for buried faults show similar trends, while curves for faults reaching the free surface are quite different (Fig. 8c). Let us consider buried faults first. As the fault depth decreases, R_1 increases, faster for strike-slip than dip-slip faults, and shows a more pronounced dependence on the dip angle (nearly absent for very deep faults). Independently of fault depth, when $\delta \approx 15°$–$20°$ all the curves seem to approach a common value.

The ratio R_1 reaches the greatest values for an outcropping vertical strike-slip fault and for an outcropping, shallow-dipping dip-slip fault (Fig. 8c). The dependence of R_1 on the fault aspect ratio L/W has been studied for faults with their upper edge at 1 km depth. Fig. 9(a) shows that, for a typical strike-slip fault, almost vertically dipping, the ratio R_1 is maximum for $L/W \approx 1$–1.5. For typical normal dip-slip faults the ratio R_1 reaches a maximum at $L/W \approx 1.5$–3 for high dip angles and at $L/W \approx 5$ for an almost vertical dip angle. The maximum R_1 value is, however, for typical thrust faults (shallow dipping) with aspect ratio $L/W > 1$. For neither strike-slip or dip-slip faults does the ratio R_1 increase for $L/W < 0.5$ and $L/W > 10$.

Another ratio, $R_2 = \max|D_\perp / D_\parallel|$, is worthy of mention. For buried faults, its value is typically

$$R_2 = \max|D_\perp / D_\parallel| \approx 7-15 \text{ per cent},$$

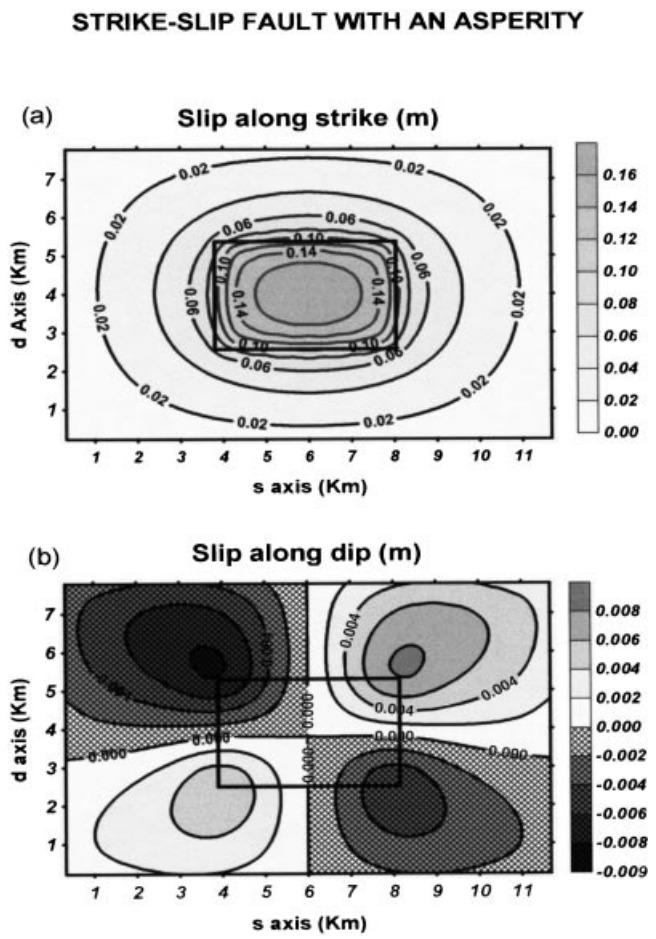

Figure 6. Same as Fig. 4, for a vertical fault with 3 MPa stress release in the strike direction, limited within a rectangular 4×3 km^2 central asperity, while the rest of the fault slips with vanishing stress drop.

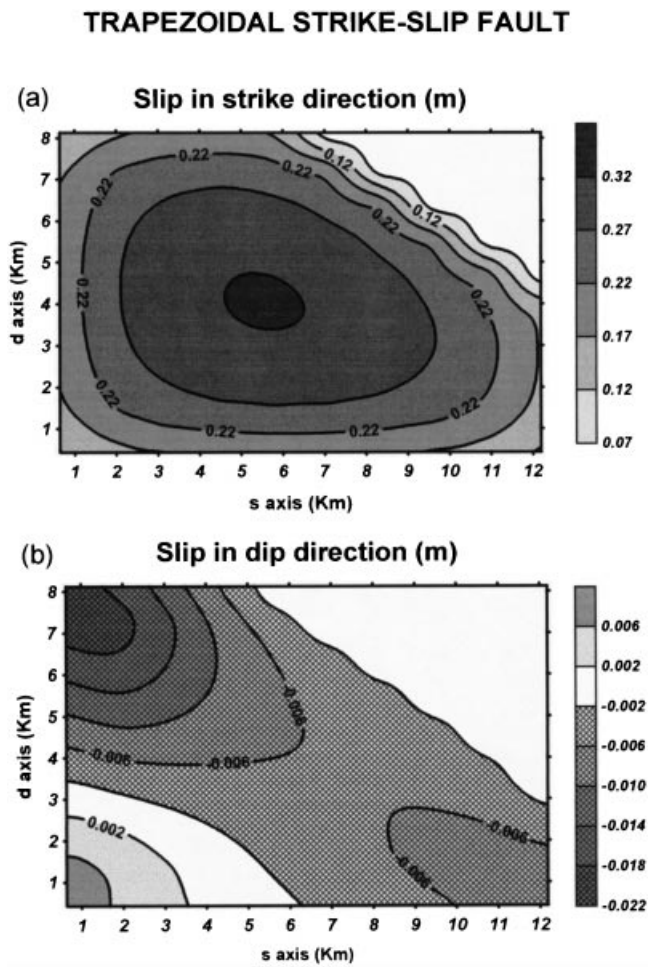

Figure 7. Slip along strike (a) and dip (b) for a vertically dipping trapezoidal fault surface with upper edge at a depth of 1 km and releasing 2.5 MPa in the strike direction. With respect to Fig. 4, fault dimensions have been adjusted in order to have the same area with non-vanishing slip ($L_{\text{bottom}} = 13.86$ km, $L_{\text{top}} = 6.93$ km, $W = 9.24$ km).

while for outcropping faults,

$$R_2 = \max|D_\perp / D_\parallel| \approx 10 - 40 \text{ per cent}.$$

The maximum values are near the upper corners of the fault and may cause a variation up to 20° in the slip rake. The trend of the curves for R_2 resembles that of the ratio R_1. These results are plotted in Fig. 10. The maximum of R_2 is always on elements near the fault edges. Here the values of $D_\parallel$ and $D_\perp$ may be small, despite a high value of R_2. Accordingly, $\max(R_2)$ may depend somewhat on the refinement of the fault plane subdivision.

In Figs 8–10 and in some of the figures that follow, some sharp variations of trend are present. These may have two causes. As the dip angle varies, absolute maxima may move from a relative maximum to a different one, giving rise to sharp changes in R_1 or R_2; minor changes are typically due to relative maxima jumping from one element to the next and might accordingly become smoother by increasing the number of elements.

As an example, consider Fig. 10(a). The curve for an outcropping fault shows a very sharp cusp near $\delta = 60°$. We checked that at this angle the maximum of R_2 jumps from the element $k = 1$ (bottom) to the element $k = 100$ (shallow) so that the curve is composed of a segment of R_2 computed on element $k = 1$ and a segment of R_2 computed on element $k = 100$; no significant smoothing can be obtained in this case by employing a greater number of elements.

FAULT PLANE DEFORMATION

The numerical model above allows us to study in some detail the fault plane deformation after an earthquake. This problem has received little attention up to now, probably because no such effect is present for infinitely long faults for which simple analytical solutions exist. This deformation can be computed interpolating the normal displacement calculated on each centre point of the elements comprising the fault plane.

Fig. 11 shows how the fault plane is deformed by the continuous normal component of displacement, u_t (u_t should not be confused with the discontinuous displacement D_t, which is assumed to vanish. The displacement of the fault plane consists mainly of a small *rotation* around an axis normal to the released traction and a *bending* of the originally plane fault

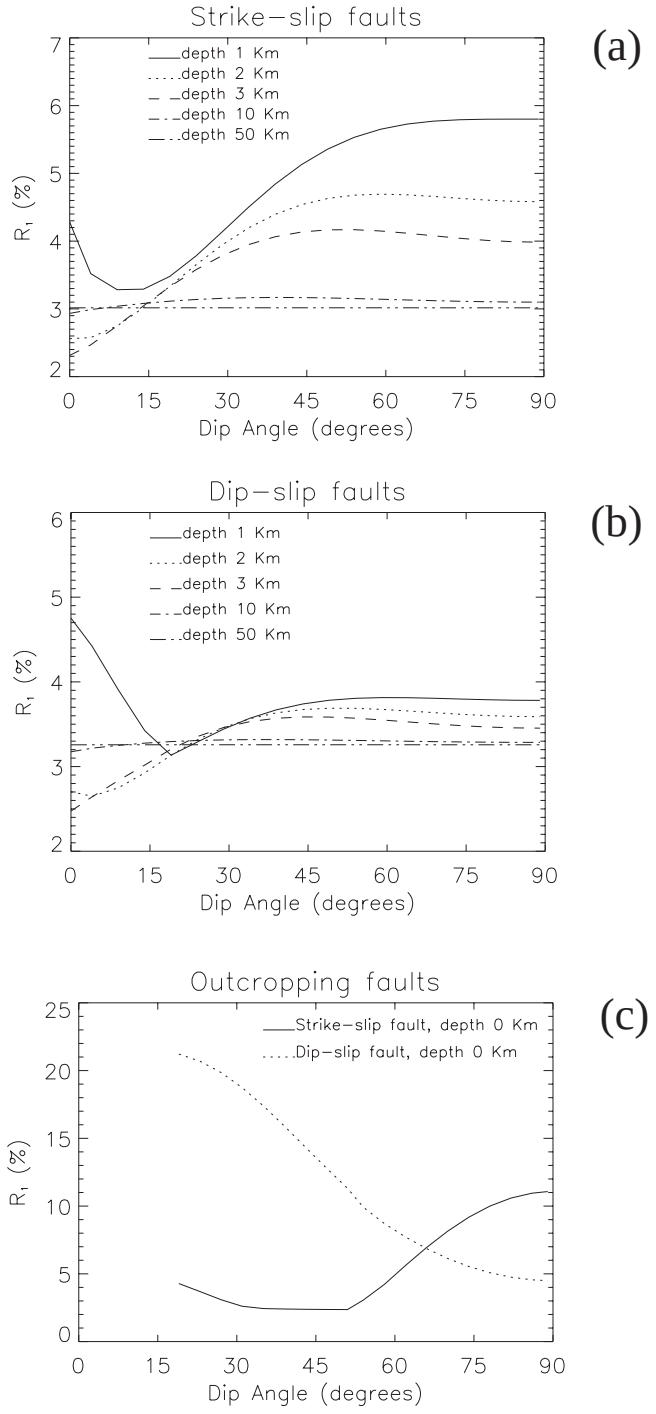

Figure 8. Plots of the ratio $R_1 = \max|D_\perp| / \max|D_\parallel|$ as a function of dip angle for (a) strike-slip faults at different depths, (b) dip-slip faults at different depths, and (c) strike-slip and dip-slip surface faults. The stress drop is 2.5 MPa and fault dimensions are $L = 12$ km, $W = 8$ km.

surface. Consider the direction defined by the *main* slip D_s (for Fig. 11a) or D_d (in 11b) and let $s = a$ or $d = a$, respectively, be the fault plane rotation axes. We define the s' or d' axes as having their origin on the straight line $s = a$ or $d = a$ and oriented in the direction of the main slip D_s or D_d, respectively. Looking at the fault surface from $t > 0$ we identify two areas:

(1) fault plane *front area*; $s' > 0$ or $d' > 0$;
(2) fault plane *back area*; $s' < 0$ or $d' < 0$.

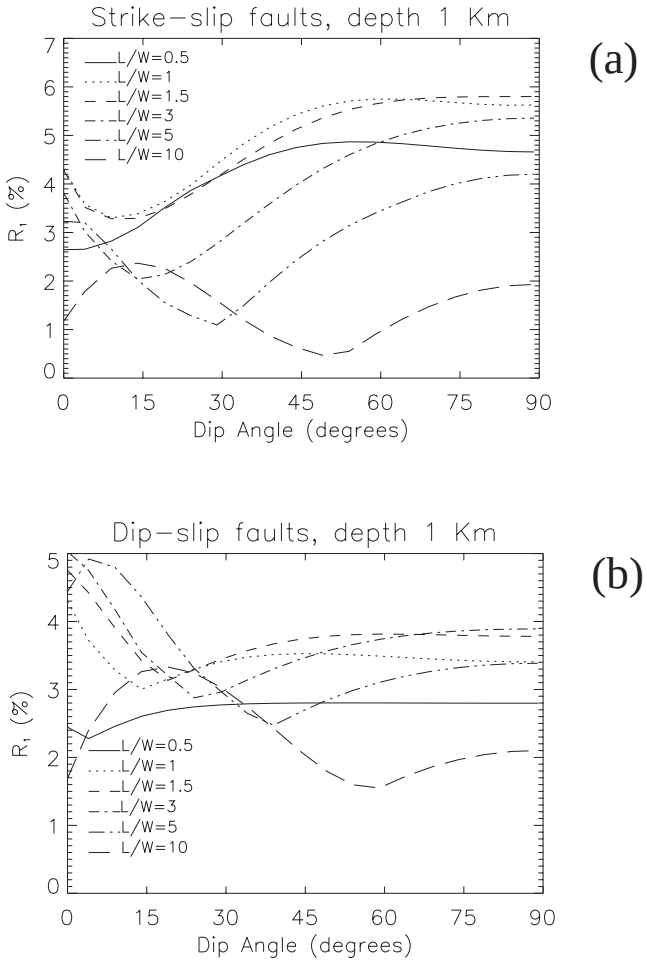

Figure 9. Plots of the ratio $R_1 = \max|D_\perp| / \max|D_\parallel|$ as a function of dip angle for different aspect ratios L/W. (a) Strike-slip faults, (b) dip-slip faults with upper edge at 1 km depth and stress drop of 2.5 MPa.

Using the above conventions, the results on fault deformation show that

(1) the front area moves in the $t > 0$ direction; we say that it *uplifts*;
(2) the back area moves in the $t < 0$ direction; we say that it *subsides*.

This normal displacement has greater amplitude on the shallower section of the fault surface. The mean ratio between the maximum normal displacement (in absolute value), $|u_t^{\max}|$, and the maximum slip, $|D_\parallel^{\max}|$, is found to be typically less than 20 per cent. Values of the ratio $R_3 = |u_t^{\max}| / |D_\parallel^{\max}|$ are plotted in Fig. 12. The deformation grows as the fault depth decreases. R_3 is more sensitive to depth for typical dip-slip faults than for typical (vertical) strike-slip faults.

The deformation of the fault plane induced by the occurrence of an earthquake may need a few words of comment. The rotation of the fault plane in Fig. 11 may seem opposite to what is expected intuitively, given the slip direction. However, this rotation is easily understood in terms of the distribution of double couples, which are equivalent to the given dislocation. The non-uniform distribution of slip is responsible for a non-uniform distribution of force couples. Force couples normal to the fault plane are responsible for the rotation of the fault

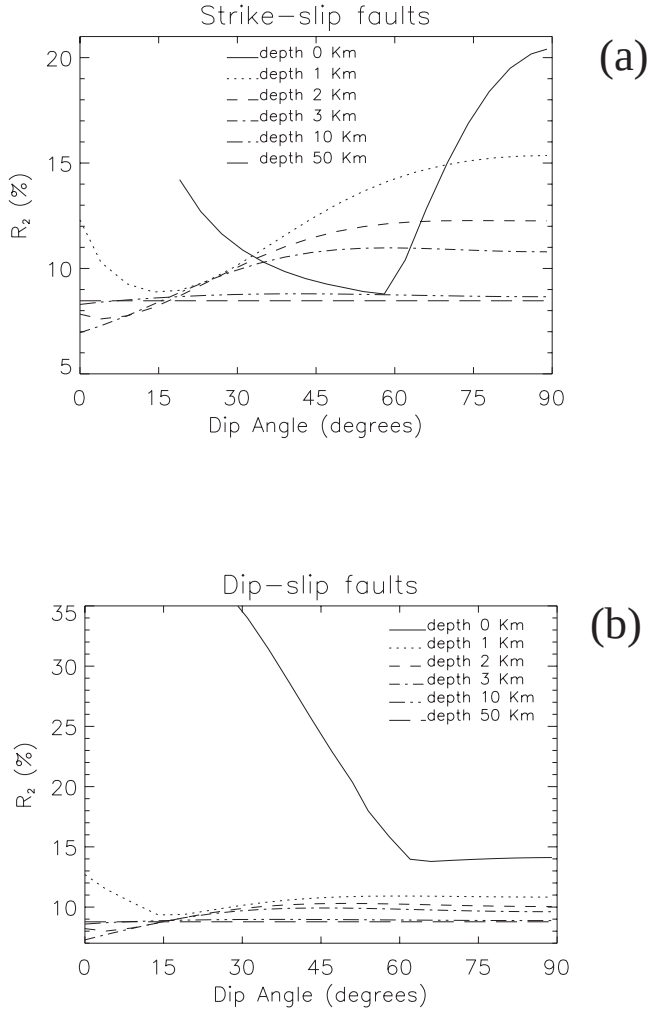

Figure 10. Plots of the ratio $R_2 = \max|D_\perp / D_\parallel|$ as a function of dip angle for (a) strike-slip faults and (b) dip-slip faults at different depths (referred to the upper fault edge). The stress drop is 2.5 MPa and fault dimensions are $L = 12$ km, $W = 8$ km.

plane, while their non-uniform intensity is responsible for the fault concavity/convexity (see e.g. Aki & Richards 1980, Chapter 3). In Fig. 11 the balancing force couples normal and parallel to the fault plane are shown qualitatively by vertical and horizontal arrows respectively.

It must be mentioned that the rotation of the fault plane was correctly reproduced in previous far-field analyses (e.g. Chinnery 1961, 1963; Press 1965), but no mention was made of this effect, probably due to the negligibly small values of rotation. The fault plane deformation might seem insignificant, amounting to a few centimetres compared to typical fault dimensions (here ≈ 10 km). However, these effects may accumulate for subsequent earthquakes on the same fault or nearby faults and may give rise to significant fault indentation. If the stress drop on the fault is strongly heterogeneous, as is often the case in real earthquakes, the deformation is found to concentrate around heterogeneities, giving rise to further undulations of the fault surface. The normal component of displacements is moreover accompanied by large normal stresses, which are probably the most relevant effects produced by the interaction between fault plane and free surface, as discussed below.

SELF-INDUCED NORMAL STRESS

The normal traction $t_t'^{(k)}$, $k = 1, \ldots M \times N$, that develops on the fault after a slip event will be called the *self-induced* normal stress field. The main features of this stress component are as follows:

(1) the normal traction is *absent* on vertical faults (either strike-slip or dip-slip), or on inclined very deep faults;
(2) its absolute value is larger on the more deformed and shallower areas;
(3) it increases considerably as the fault approaches the free surface;
(4) its pattern is similar to that of the normal displacement. After the earthquake, there is *extension* in the fault area that uplifts (*front area*) and *compression* in the area that subsides (*back area*).

In Fig. 13 the normal stress field is plotted on (a) a strike-slip fault dipping at 60° and (b) on a dip-slip fault dipping at 30°.

We define the ratio

$$R_4 = \frac{\max|t_t'|}{|\Delta\sigma|},$$

where $\max|t_t'|$ is the maximum intensity of self-induced normal stress and $\Delta\sigma$ is the stress drop as defined in (2). In Figs 14(a) and (b) the ratio R_4 as a function of the fault dip angle is plotted for faults at different depths.

The normal stress field is not negligible. In the more realistic cases of Fig. 14, it can be 10 per cent of the stress drop for buried strike-slip faults (typically dipping with $\delta > 75°$), 50 per cent for buried dip-slip faults and even 120 per cent for a dip-slip fault with $\delta = 60°$ (typical normal fault) that reaches the free surface. From Fig. 14 it can be inferred that this field is due to the interaction between the fault deformation and the free surface. Consider t_t' as given by the elastic deformation in the local system (s, d, t):

$$t_t' = (\lambda + 2\mu)\frac{\partial u_t}{\partial t} + \lambda\left(\frac{\partial u_s}{\partial s} + \frac{\partial u_d}{\partial d}\right), \tag{9}$$

where (u_s, u_d, u_t) is the displacement field. It can be shown that the term containing $(\lambda + 2\mu)$ always prevails over the term containing λ and is mostly responsible for the pattern and intensity of the normal stress field. If the term multiplied by λ is neglected, it can be seen that the self-induced normal stress is mainly caused by the gradient in the normal direction t of the normal displacement u_t on the fault plane. This gradient is non-vanishing for inclined faults and is caused by the different behaviour of the regions lying above and below the fault. In other terms, the hangingwall block above the fault deforms much more easily than the footwall block. For a *vertical* fault, the normal displacement is horizontal and since the half-space is horizontally homogeneous, the gradient $\partial u_t / \partial t$ vanishes by symmetry over the fault plane.

DISCUSSION

The self-induced normal stress may influence the fault behaviour during slip or in the post-seismic phase. Suppose that the fault undergoes shear failure following the Coulomb criterion:

$$|\tau| + f(\sigma_n + p) \geq S_0, \tag{10a}$$

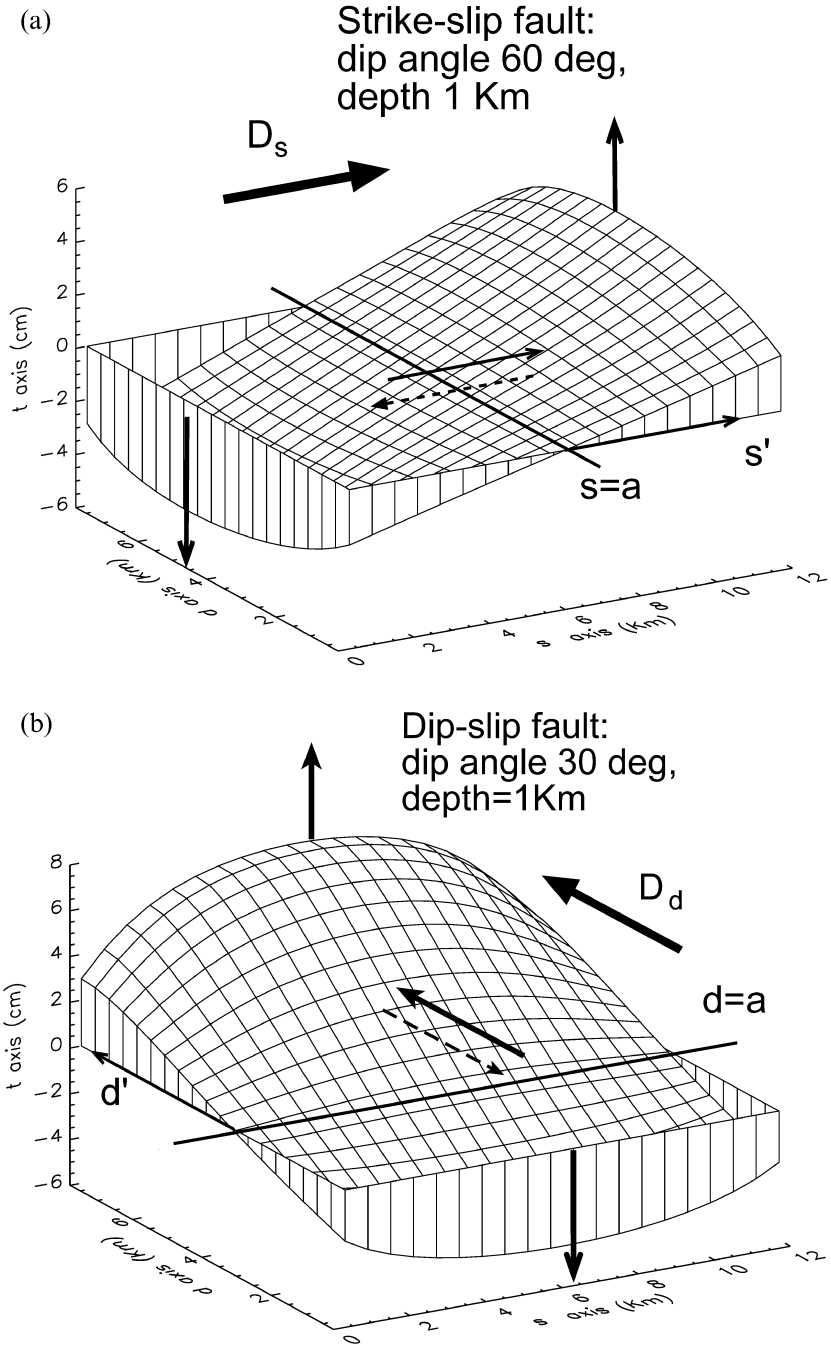

Figure 11. Fault plane deformation after the earthquake on (a) a strike-slip fault at a depth of 1 km dipping at 60° and (b) a surface thrust fault dipping at 30°. Deformation is plotted with respect to the undeformed fault plane $t=0$. A qualitative scheme is also shown for the system of forces responsible for the fault plane deformation (vertical arrows), the second couple of forces (horizontal arrows), the maximum slip direction and the axis of fault plane rotation ($s=a$, $d=a$). The stress drop is 2.5 MPa and fault dimensions $L=12$ km, $W=8$ km.

where τ is the shear stress, f is the friction coefficient, σ_n is the normal stress (negative if compressive) on the fault plane, p is the pore pressure and S_0 is a positive constant that may be regarded as the inherent shear strength of the material. If the medium is isotropic, Skempton (1954) showed that the pore pressure change in undrained conditions is related to the stress change in the solid matrix according to

$$\Delta p = -\frac{B}{3}\Delta\sigma_{kk}\,,$$

where B is the Skempton parameter ($B=1$ for incompressible rock–fluid constituents). It has been suggested (Rice 1992; Harris 1998) that $\Delta p \propto \Delta\sigma_n$ in fault zones, so that eq. (10) may be rewritten incorporating Δp into an effective friction coefficient $f' < f$ in the following way:

$$|\tau| + f'\sigma_n \geq S_0\,. \tag{10b}$$

Version (10b) of the failure criterion has been employed by e.g. Stein *et al.* (1992) and King *et al.* (1994). In this section we shall

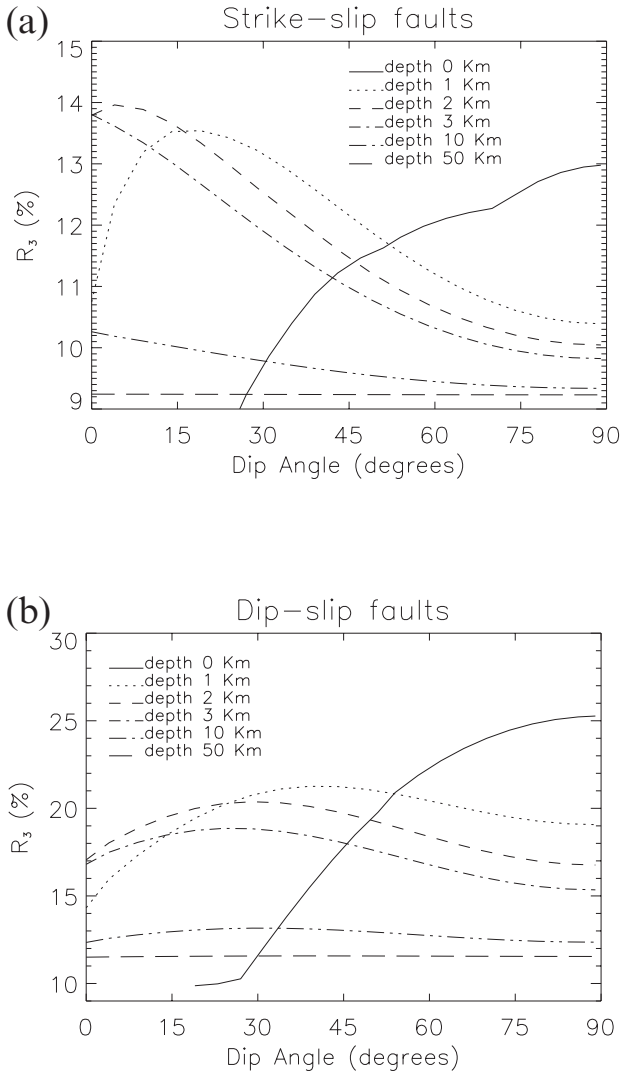

Figure 12. Fault plane deformation: plots of the ratio $R_3 = \max|u_t / D_{\|}|$ as a function of dip angle for (a) strike-slip faults and (b) dip-slip faults of different depths. The stress drop is 2.5 MPa and fault dimensions $L = 12$ km, $W = 8$ km.

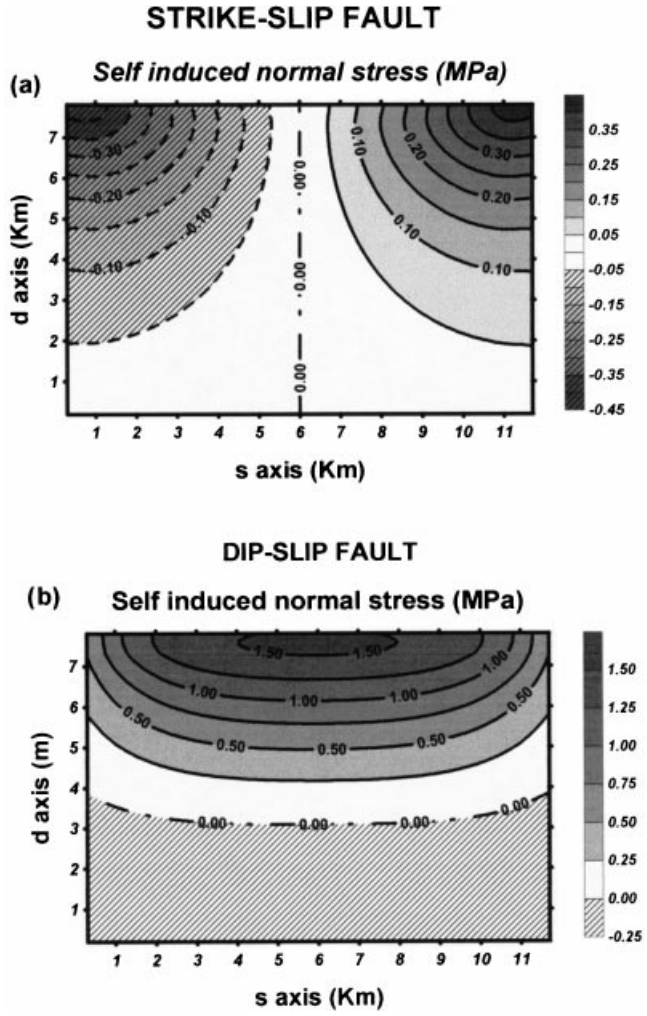

Figure 13. Self-induced normal stress on the fault plane of (a) a strike-slip fault and (b) a dip-slip fault. Fault parameters are the same as in Fig. 4.

employ the failure criterion (10b) but in the following section we shall also employ the criterion (10a).

During the slip, a fraction $\Delta\tau$ of the total shear stress τ is released and a normal stress $\Delta\sigma_n$ is induced. After the earthquake the failure condition (10b) is

$$|\tau + \Delta\tau| + f'(\sigma_n + \Delta\sigma_n) \geq S_0\,, \tag{11}$$

where we assume that f' and S_0 do not change following the earthquake. The *Coulomb failure function* is defined as

$$CFF = |\tau| + f'\,\sigma_n\,. \tag{12}$$

Let us assume $\tau > 0$. Then $\Delta\tau$ (the stress drop) is usually negative over the fault plane, but it might be positive on some elements if the slip is highly inhomogeneous. In the present section we shall consider a constant stress drop on the fault plane, so that

$$\Delta\tau = -|\Delta\sigma| \qquad \text{on the fault plane}\,,$$

where $\Delta\sigma$ is the stress drop as defined in (2).

If we furthermore say that $|\Delta\sigma| < |\tau|$, the change ΔCFF due to the earthquake is

$$\Delta CFF = -|\Delta\sigma| + f'\,\Delta\sigma_n\,. \tag{13}$$

Regions where $\Delta CFF > 0$ are left nearer to failure than they were before the earthquake, while regions where $\Delta CFF < 0$ should be strengthened. Then, changes in the Coulomb failure function computed over the fault surface in the absence of self-induced normal stress, say ΔCFF^0, are always *negative* in constant stress drop models,

$$\Delta CFF^0 = -|\Delta\sigma| < 0\,,$$

and accordingly, after the earthquake, all the fault would be further from failure. It should be noted that the opposite takes place in the prolongation of the fault surface beyond the slipped region.

In the numerical model discussed in the previous section the normal stress field on the kth element is proportional to the shear stress release $\Delta\sigma$ (from eq. 6):

$$\Delta\sigma_n^k = \alpha^k |\Delta\sigma|\,, \tag{14}$$

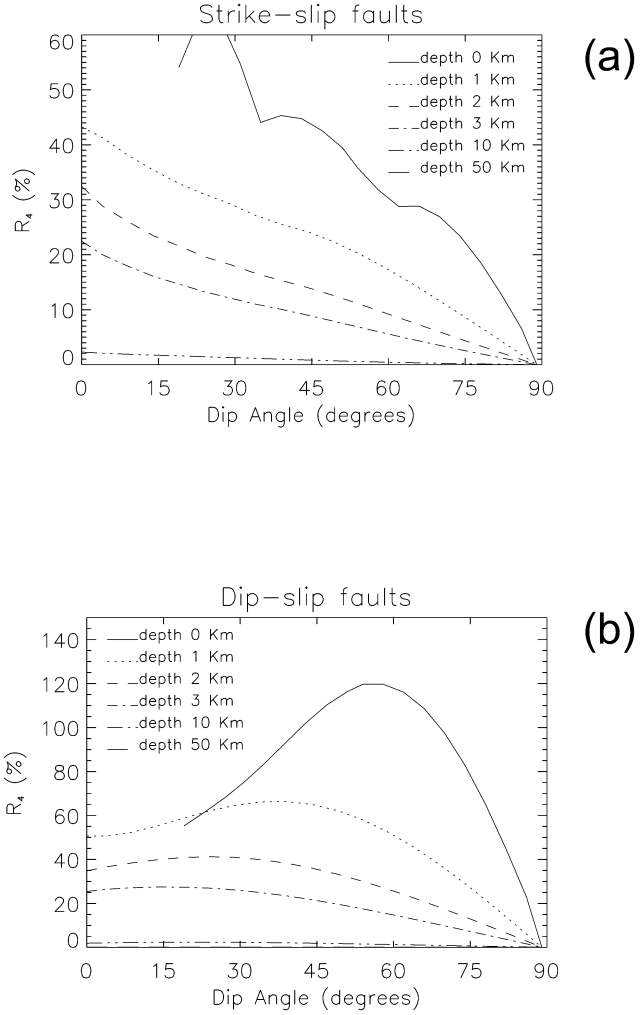

Figure 14. Plots of ratio $R_4 = \max|t'_t|/|\Delta\sigma|$, where $\max|t'_t|$ is the maximum absolute value of self-induced normal stress and $|\Delta\sigma|$ is the stress drop as defined in (2), as a function of a dip angle on (a) strike-slip faults and (b) dip-slip faults of different depths. The stress drop is 2.5 MPa and fault dimensions $L = 12$ km, $W = 8$ km.

where α^k is positive in 'uplifted' fault portions and is negative in 'subsiding' fault portions. When self-induced normal stress is considered, ΔCFF is found by inserting (14) into (13):

$$\Delta CFF = -|\Delta\tau|(1 + \alpha f'), \tag{15}$$

where the index k is omitted for brevity. Using $f' = 0.85$, a value typical for rocks in laboratory tests (Byerlee 1977), and $\alpha \approx \pm 0.5$, which is a typical maximum value for shallow dip-slip faults according to Fig. 14(b), we find $\alpha f' \approx \pm 0.4$. The factor $\alpha f'$ is able to amplify or decrease ΔCFF by ≈ 40 per cent with respect to ΔCFF^0. Normal *compressive* self-induced stress generates a stronger decrease of Coulomb stress, $\Delta CFF < \Delta CFF^0 < 0$, which brings the fault further from failure. Normal *extensional* self-induced stress causes a minor decrease of the Coulomb stress, $\Delta CFF > \Delta CFF^0$, which might even be an increase under favourable circumstances. In the latter case the fault would move closer to failure.

To be more specific, let us consider dip-slip faults. According to the numerical models presented, a *thrust* fault mainly develops extensional stress while a *normal* fault mainly develops *compressive* stress. Both are maxima in absolute value in the surficial fault portion (Fig. 15). As a first observation it can be stated that the occurrence of an earthquake always leads the shallower section of a normal fault towards a more stable equilibrium than a thrust fault. In the case of buried faults, the absolute value of normal stress is maximum for intermediate and shallow dip angles, whilst it vanishes as $\delta \to 90°$ (see Fig. 14b). Following the above considerations about ΔCFF, we are lead to conclude that

(1) *thrust* faults with a dip shallower than 45° are favoured to slip again in the post-seismic phase;

(2) *normal* faults with a dip shallower than 60° are strengthened and post-seismic slip is likely to occur for higher dip angles.

These results are in rough agreement with those predicted by Anderson's theory of faulting and suggest that cumulative effects after several seismic cycles tend to favour low-dip thrust faults and high-dip normal faults.

The present computations suggest that Coulomb stress changes caused by self-induced normal stress may influence significantly future fault activity. In fact, extensional stress

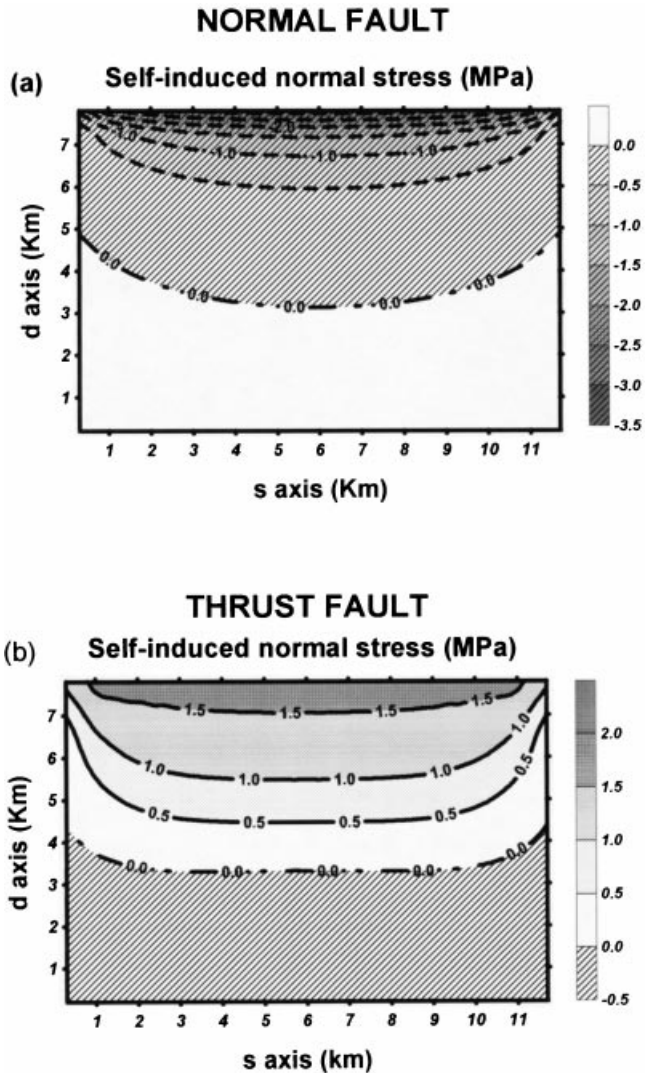

Figure 15. Self induced normal stress on (a) an outcropping normal fault dipping at 70° and (b) an outcropping thrust fault dipping at 30°. The stress drop is 2.5 MPa and fault dimensions $L = 12$ km, $W = 8$ km.

in the front area of the fault and compressive stress in the back area leave these areas in a less stable and more stable equilibrium, respectively. In the front area aftershocks or future stress release would occur, while the back area would be moved further from failure.

As a consequence, very shallow seismic activity can be expected in the post-seismic phase on thrust faults, while the shallowest portion of normal faults should be frictionally stable. In the long-term, due to cumulative effects, seismicity on thrust faults is expected to be shallower than on normal faults, as long as brittle rheology is assumed. However, in the ductile regime this effect may be cancelled or reversed since extensional regions, which are generally sites of normal earthquakes, are generally associated with high heat flow, which shifts the brittle–ductile transition to shallower depths.

We consider also the case of a thrust fault reaching the free surface. In Fig. 16 the maximum extension or compression computed on horizontal stripes of different depths is plotted as a function of the dip angle. The maximum extension in deeper areas is for $0^\circ < \delta < 30^\circ$. At great depths, thrust faults dipping at these angles are favoured by the stress field left by previous events. In the 2–3 km below the free surface, the maximum extension is for $30^\circ < \delta < 60^\circ$. From this result one might infer that, in the most surficial area, the fault surface may vary its dip from a value $\delta = 30^\circ$ at depth to $\delta \geq 60^\circ$ near the surface, in order to follow the path that minimizes normal compression (i.e. friction). Such a bending of thrust faults near the free surface is commonly observed in the field or from seismic prospecting (e.g. Finetti *et al.* 1979). The same upward-concave bending is predicted for normal faults, typically with a dip greater then 60°, since high compression is induced on shallow strips with this dip while the minimum compression is found for vertically dipping strips.

FIELD EVIDENCE

In this section we present a few examples that seem to support a significant role being played by self-induced normal stress in the post-seismic phase, as discussed in the previous section. An interesting data set refers to four seismic sequences located in the proximity of the Italy–Slovenia border, accurately located thanks to the presence of local and mobile seismic networks connected to the permanent national Italian seismic network. Accurate hypocentre determinations of these sequences are given by Bressan et al. (1999). Three seismic sequences were in the thrust domain of the Friuli region (NE Italy) with main shocks taking place respectively on 1988 February 1 ($M = 4.2$), 1991 October 5 ($M = 3.9$) and 1996 April 13 ($M = 4.3$); the fourth sequence—1998 April 12 ($M = 5.6$)—was in western Slovenia, and in spite of the short distance from the previous sequences, was located in the strike-slip domain. In Fig. 17, focal mechanisms of the main events are shown, together with main shock and aftershock hypocentres. From the discussion in the previous section we should expect that, other things being equal, thrust fault earthquakes should be followed by shallow aftershocks due to the lower friction produced by self-induced tensile normal stress (see Fig. 13b) concentrated near the surface. No self-induced stress is present on a vertical strike-slip fault so that aftershock hypocentres after the fourth (strike-slip) earthquake should not show any preference for shallower depth. This is actually found to be the case for the data sets in Fig. 17.

In the 1997 Umbria–Marche seismic sequence (central Apennines), two main shocks very close in time and space (with $M_w = 5.7$ and 6.0) on 1997 September 26 were followed by thousands of aftershocks, several of which were located very close to the normal fault plane, dipping 45° towards the SW (Amato *et al.* 1998). The main shock hypocentres were approximately in the middle of the aftershock distribution (Fig. 4 in Amato *et al.* 1998) but the rupture mechanisms inferred from near-source strong motion records (Zollo *et al.* 1999) show up-dip rupture propagation for both events, with maximum slip taking place 3–4 km up-dip of the nucleation point. Accordingly, among the aftershocks located next to the fault plane, many more took place on the deeper fault section than on the shallower section, in agreement with the increased friction inferred in the previous section for the shallow part of

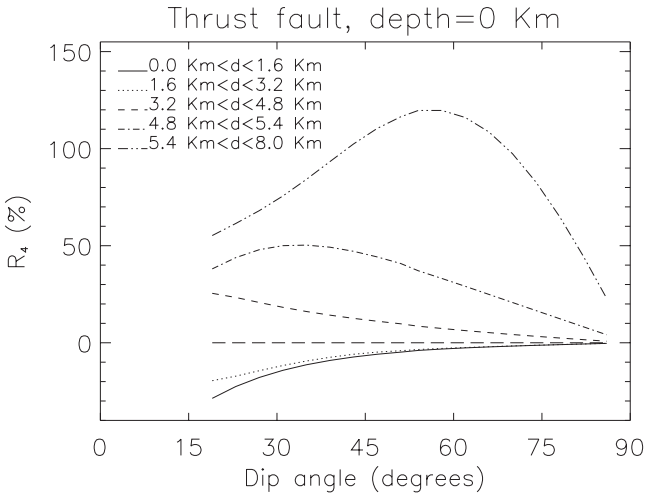

Figure 16. Self-induced normal stress t'_t as a function of the dip angle on horizontal stripes of the fault plane. A surface thrust fault is considered. The ranges of d in the plot represent the stripe extension along the d axis (see Fig. 1); *shallower* stripes have greater d values. The stress drop is 2.5 MPa and fault dimensions are $L = 12$ km, $W = 8$ km.

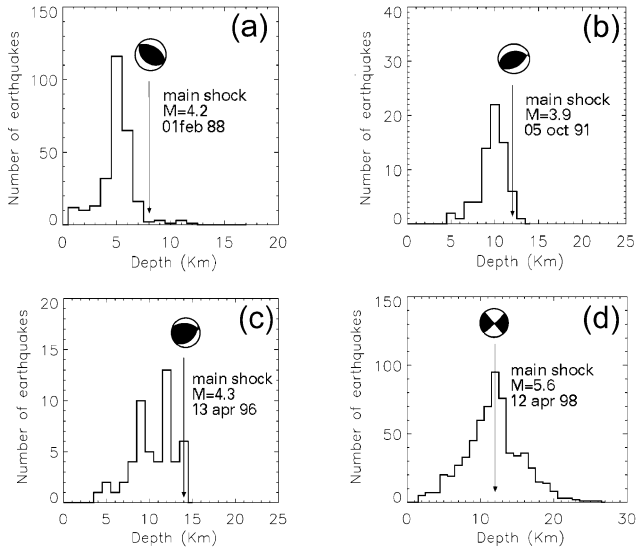

Figure 17. Hypocentre distribution of aftershocks of three thrust fault earthquakes in NW Italy (a, b and c) and one strike-slip earthquake in western Slovenia (d). The main shock depths and focal mechanisms are indicated (redrawn after Bressan, G. *et al.* 1999).

a normal fault. According to the present model, however, we should also expect very shallow aftershocks to be inhibited by increasing friction on the shallowest fault section, which does not seem to be the case in the data set. This partial failure might be explained in terms of induced (positive) pore pressure in compressive regions or in terms of the large heterogeneities present in shallower layers, or else in terms of a shear stress increase produced by highly variable slip over the fault plane or by stress concentration just outside the fault plane. In other words, it must be stated clearly that the self-induced normal stress is not claimed to be the only parameter governing aftershock occurrence.

Finally, we shall consider the 1983 $M=7.3$ Borah Peak (Idaho) seismic sequence for which a detailed slip distribution is available for the main shock (Mendoza & Hartzell 1988). The earthquake occurred on an outcropping normal fault dipping at 50°. From the slip distribution, the induced stresses can be computed according to eqs (6)–(7). The slip distribution shows regions with high variability, where positive shear stress changes can be induced. In Fig. 18(a) the effective normal stress,

$$\Delta\sigma_n^{\text{eff}} = \Delta\sigma_n - B\,\frac{\Delta\sigma_{kk}}{3}\,, \tag{16}$$

is plotted (positive values involve extension, negative values involve compression). Most aftershocks are concentrated in regions of positive $\Delta\sigma_n^{\text{eff}}$, where friction is lowered after the main shock. In Fig. 18(b) the change in the Coulomb failure function ΔCFF is plotted, as given by $\Delta\tau+\Delta\sigma_n^{\text{eff}}$ (consistent with version 10a of the failure criterion). ΔCFF is dominated by the shear stress change $\Delta\tau$, and essentially the same pattern would be produced from (10b). Aftershocks seem to stay away from high negative ΔCFF areas of the fault plane, but no clear concentration inside positive ΔCFF regions is evident. This might give support to the hypothesis that the unclamping effect of positive $\Delta\sigma_n^{\text{eff}}$ can be more important than the shear stress in triggering instability, as also suggested by Perfettini *et al.* (1999).

CONCLUSIONS

Numerical models of a shear fault with constant stress drop and variable slip suggest that an earthquake can change significantly the state of normal stress on the fault plane itself, particularly at shallow depth. The self-induced normal stress depends critically on fault mechanism and fault geometry (dip, depth, aspect ratio) and is not uniform over the fault plane.

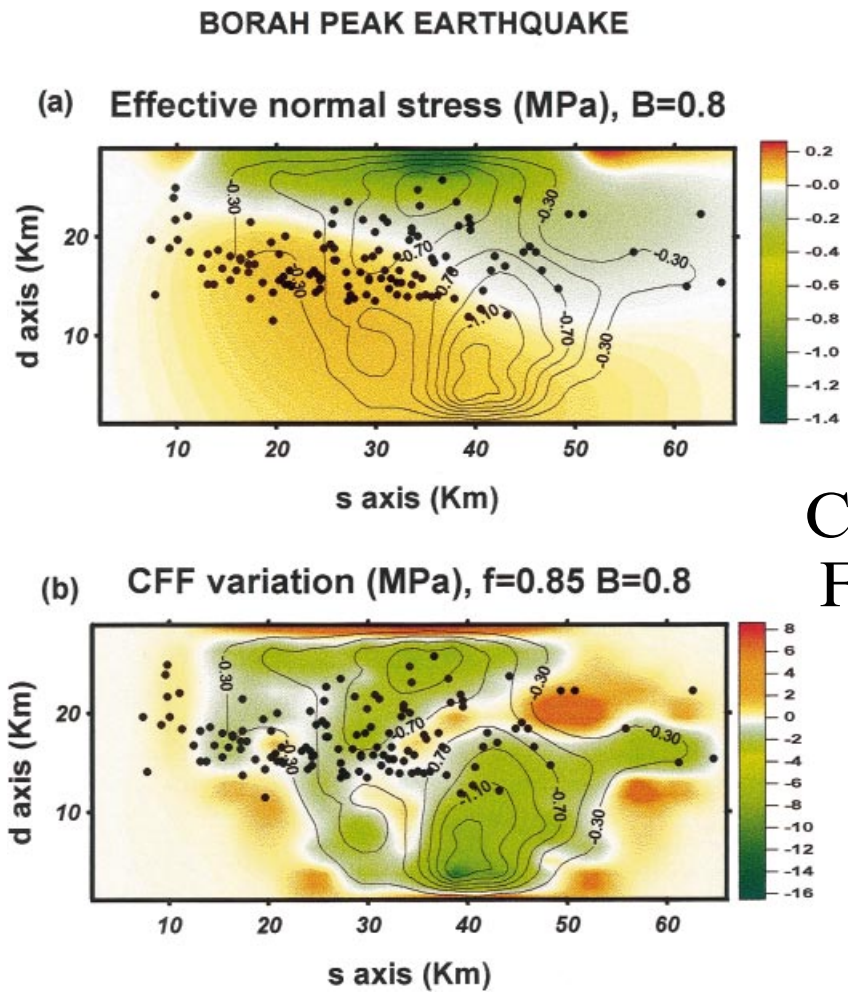

COLOUR FIGURE

Figure 18. (a) Effective normal stress variation $\Delta\sigma_n - B\Delta\sigma_{kk}/3$ (eq. 10a) computed from the Mendoza–Hartzell (1988) slip model of the 1983 Borah Peak earthquake with $B=0.8$. Thin lines show the slip contours, black dots show aftershock locations on the fault plane. (b) Coulomb failure function variation ΔCFF for the same earthquake computed from (10a) with friction coefficient $f=0.85$ and $B=0.8$.

If normal stress changes are neglected, a shear stress drop, uniform over the fault plane, should always lead to a situation of more stable equilibrium. If self-induced normal stresses are taken into account, according to the Coulomb failure function, we see that different fault areas are brought to different states of equilibrium following the earthquake. Thrust faults become weaker in their shallow regions, while normal faults become stronger. No self-induced normal stress is present on typical (vertical) strike-slip faults. After the earthquake, the originally plane fault surface undergoes a rotation and a deformation (strictly related to the self-induced stress) that may significantly perturb an originally straight tectonic margin. These effects are typically small for a single event but may be significant for a sequence of several events, even if anelastic deformation must be taken into account in the long term. In general, self-induced extension cannot by itself produce positive values for ΔCFF, but it may contribute to generate positive ΔCFF in regions of high stress gradient (Fig. 18b). Its plausible effect is to decrease the repeat time of the next shock; Perfettini *et al.* (1999) also proposed that a tensile normal stress may affect significantly the slip amplitude by unclamping the fault.

Among the models presented, those characterized by uniform traction release are clearly oversimplified with respect to real faulting events. The uniform stress drop models constitute only a preliminary step to understanding the physics of permanent self-induced effects. Real fault surfaces may be non-planar and bends in the fault strike can be the source of large normal stresses. Complex events may involve different fault segments with different dip and depth. Even in the case of planar faults, very heterogeneous slip distributions are often inferred from the inversion of seismic and geodetic data, which in turn require a very heterogeneous stress drop. As mentioned in the previous section, these heterogeneities can be responsible for positive changes of $\Delta\tau$ and thus produce large positive ΔCFF on the fault plane. These complex slip distributions can be easily inserted in the boundary element model, as shown in Fig. 18 for the Borah Peak earthquake.

ACKNOWLEDGMENTS

The present work was performed with financial contribution from MURST and from the Commission of European Communities (Program Environment and Climate, project PRENLAB-2). AN was supported by a CEC fellowship within the same project under contract ENV4-CT97-0536. Thanks are due to R. S. Stein and M. Cocco for useful discussions and suggestions, to R. W. Simpson and G. De Natale for their careful reviews of a preliminary version of the present paper and to G. Bressan for providing the hypocentre data related to the Friuli–Slovenia earthquake sequences.

REFERENCES

Aki, K. & Richards, P., 1980. *Quantitative Seismology, Theory and Methods,* Freeman, San Francisco.

Amato, A. *et al.*, 1998. The 1997 Umbria-Marche, Italy, earthquake sequence: a first look at the main shocks and aftershocks, *Geophys. Res. Lett.,* **25,** 2861–2864.

Becker, T.W. & Schmeling H., 1998. Earthquake recurrence time variations with and without fault zone interactions, *Geophys. J. Int.,* **135,** 165–176.

Bressan, G., Bragato, B.L. & Govoni, A., 1999. Aftershock sequence analysis using a static fatigue approach, *Boll. Geofis. Teor. Appl.,* in press.

Byerlee, J.D., 1977. Friction of rocks, in *Experimental Studies of Rock Friction with Application to Earthquake Prediction,* pp. 55–77, ed. Evernden, J.F., USGS, Menlo Park, CA.

Chinnery, M.A, 1961. The deformation of the ground around surface faults, *Bull. seism. Soc. Am.,* **51,** 355–372.

Chinnery, M.A., 1963. The stress changes that accompany strike-slip faulting, *Bull. seism. Soc. Am.,* **53,** 921–932.

Crouch, S.L. & Starfield, A.M., 1983. *Boundary Element Method in Solid Mechanics,* Unwin Hyman, London.

Finetti, I., Russi, M. & Slejko, D., 1979. The Friuli earthquake, *Tectonophysics,* **53,** 261–272.

Fung, Y.C., 1965. *Foundations of Solid Mechanics,* Prentice Hall, Englewood Cliffs, NJ.

Harris, R.A., 1998. Introduction to special section: stress triggers, stress shadows and implications for seismic hazard, *J. geophys. Res.,* **103,** 24 347–24 358.

Jaeger, J.C. & Cook, N.G.V, 1979. *Fundamentals of Rock Mechanics,* Chapman & Hall, London.

Kasahara, K., 1981. *Earthquake Mechanics,* Cambridge University Press, Cambridge.

King, G.C.P., Stein, R.S. & Lin, J., 1994. Static stress change and the triggering of earthquakes, *Bull. seism. Soc. Am.,* **84,** 935–953.

Knopoff, L., 1958. Energy release in earthquakes, *Geophys. J. R. astr. Soc.,* **1,** 44–52.

Mendoza, C. & Hartzell, S.H., 1988. Inversion for slip distribution using teleseismic P waveforms: North Palm Springs, Borah Peak, and Michoacan earthquakes, *Bull. seism. Soc. Am.,* **78,** 1092–1111.

Nostro, C., Cocco, M. & Belardinelli, M.E., 1997. Static stress changes in extensional regimes: an application to southern Apennines (Italy), *Bull. seism. Soc. Am.,* **87,** 234–248.

Oglesby, D.D., Archuleta, R.J. & Nielsen, S.B., 1998. Earthquakes on dipping faults: the effects of broken symmetry, *Science,* **280,** 1055–1059.

Okada, Y., 1992. Internal deformation due to shear and tensile faults in a half-space, *Bull. seism. Soc. Am.,* **82,** 1018–1040.

Perfettini, H., Stein, R.S., Simpson, R.W. & Cocco, M., 1999. Stress transfer by the 1988–1989 M = 5.3 and 5.4 Lake Elsman foreshocks to the Loma Prieta Fault: unclamping at the site of peak mainshock slip, *J. geophys. Res.,* **104,** 20 169–20 182.

Press, F., 1965. Displacements, strains, and tilts at teleseismic distances, *J. geophys. Res.,* **70,** 2395–2412.

Rice, J., 1992. Fault stress states, pore pressure distributions and the weakness of the San Andreas fault, in *Fault Mechanics and Transport Properties of Rocks: a Festschrift in Honor of W. F. Brace,* pp. 475–503, eds Evans, B. & Wong, T.-F., Academic, San Diego, CA.

Shi, B., Anooshehpoor, A., Brune, J.N. & Zeng, Y., 1998. Dynamics of thrust faulting: 2D lattice model, *Bull. seism. Soc. Am.,* **88,** 1484–1494.

Skempton, A.W., 1954. The pore pressure coefficients A and B, *Geotechnique,* **4,** 143–147.

Stein, R.S., King, G.C.P. & Lin, J., 1992. Change in failure stress on the southern San Andreas fault system caused by the 1992 magnitude = 7.4 Landers earthquake, *Science,* **258,** 1328–1332.

Stein, R.S., Barka, A.A. & Dieterich, J.H., 1997. Progressive failure on the North Anatolian fault since 1939 by earthquake stress triggering, *Geophys. J. Int.,* **128,** 594–604.

Turcotte, D.L. & Shubert, G., 1982. *Geodynamics. Applications of Continuum Physics to Geological Problems,* John Wiley, New York.

Zollo, A., Marcucci, S., Milana, G. & Capuano, P., 1999. The 1997 Umbria-Marche earthquake sequence: insights on the mainshock ruptures from near source strong motion records, *Geophys. Res. Lett.,* **26,** 3165–3168.